

Supplementary Information

A. Details of theoretical model

The Landauer formula for the oscillating part of the conductance is obtained from the ray tracing scheme shown in Figure 2a of the main text. The transmission amplitude through the entire junction is taken to be a product of the transmission amplitudes at the two interfaces with a phase factor corresponding to the semiclassical phase accumulated between the junctions. This semiclassical phase difference for neighboring trajectories is

$$\theta_{WKB} = \Re \int_{-L/2}^{L/2} \sqrt{\pi|n(x)| - \left(k_y - \frac{e}{\hbar}Bx\right)^2}, \quad (1)$$

where we take the real part to account for the fact that in general the classical turning points shift from their values of $\pm L/2$ defined for $k_y = 0, B = 0$. In addition, there is a nonanalytic part of the phase associated with the vanishing of the reflection coefficients at opposite interfaces¹ which can be nontrivial at finite magnetic field,

$$\Delta\theta_{rf} = \pi \left(H\left(-k_y + \frac{eBL}{2\hbar}\right) - H\left(-k_y - \frac{eBL}{2\hbar}\right) \right), \quad (2)$$

where $H(x)$ is the step function ($H(x) = 1$ for $x > 0, H(x) = 0$ otherwise). This phase jump is equivalent to a sign change in the reflection coefficient as the incidence angle crosses zero, and implies that the transmission probability at normal incidence is unity.

At a p-n junction, assumed to be smooth on the lattice scale, the transmission amplitude is exponentially peaked about normal incidence.² The principal effect of a weak magnetic field on the transmission through a single p-n junction is to modify the incident angle at the two junctions due to cyclotron bending of the trajectories. Choosing the Landau gauge where $\vec{A} = Bx\hat{y}$ with k_y the conserved transverse momentum in the center of the junction ($x = 0$), the transmission and reflection amplitudes at the junctions located at $x = \pm L/2$ are¹

$$T_{\pm} = \exp\left(-\frac{\pi\hbar v_F}{2eE} \left(k_y \pm \frac{eBL}{2\hbar}\right)^2\right) \quad R_{\pm} = \exp(i\pi H(-k_y \mp eBL/(2\hbar))) \sqrt{1 - |T_{\pm}|^2} \quad (3)$$

Defining the total phase $\theta = \theta_{WKB} + \Delta\theta$, and taking into account the damping, due to scattering, of the particle propagators between the junctions, we can write the Landauer conductance of the heterojunction via the canonical Fabry-Perot formula as

$$G = \frac{4e^2}{h} \sum_{k_y} \left| \frac{T_+ T_- e^{-L/(2l_{LGR})}}{1 - |R_+||R_-| e^{i\theta} e^{-L/l_{LGR}}} \right|^2 \quad (4)$$

It is difficult to separate diffusive from ballistic effects in the bulk conductance. However, the contribution of diffusive effects to quantum interference effects are strongly suppressed at $B = 0$, rendering useful the definition $G_{osc} \equiv G - \bar{G}$, where \bar{G} denotes the conductance averaged over the accumulated phase. Multiple reflections are suppressed both by the finite mean free path as well as the collimating nature of the junctions; as $|T_{\pm}|, |R_{\pm}| \leq 1$, higher order products of transmission and reflection coefficients are necessarily decreasing. Utilizing this fact, we can expand the denominator in eq. (4) and subtract all nonoscillating terms to get the leading contribution to the quantum interference,

$$G_{osc} = \frac{8e^2}{h} \sum_{k_y} |T_+|^2 |T_-|^2 |R_+| |R_-| \cos(\theta) e^{-2L/l_{LGR}}. \quad (5)$$

This formula does not take into account inhomogeneities in the applied local gate potential due to the uneven width of the top gate or thickness and crystallinity of the dielectric. Such disorder can lead to significant damping of the oscillations even in a completely ballistic sample¹, and makes the estimate for the mean free path derived from matching the observed amplitude of the oscillations a lower bound. Nevertheless, that the mean free path in the LGR is shorter than that in the GL is consistent with recent experiments (unpublished) which find a strong enhancement of the Raman D-band in graphene after it is covered in HSQ and irradiated with electrons at energies and doses comparable to those used during top gate fabrication.⁴

B. Electrostatics simulations

The theoretical model described in the previous section takes as an input the potential profile across the heterojunction. In order to perform a quantitative comparison between experiment and theory, we first determine these parameters by numerical simulation of our device electrostatics using Comsol Multiphysics, a commercial finite element simulation software package. Scanning electron microscopy images of the device chosen for the quantitative comparison show the top gates to be ~ 20 nm wide, while the capacitive coupling of the top gate is found to be $C_{TG} \approx 12.8C_{BG}$. Graphene is treated as a perfect conductor covered by 10-20 nm of hydrogen silsesquioxane (HSQ), with dielectric constant $\epsilon \sim 2 - 5$, and 20 nm of HfO₂, $\epsilon \sim 10 - 15$. We choose the dielectric constant of the HSQ in each simulation to ensure a match between the calculated and measured capacitive coupling, determined as the relation between the applied top gate voltage and the maximal density reached in the LGR. The dielectric constant of atomic layer deposition (ALD) grown HfO₂ layer was consistent with a separate capacitance measurement on a similarly prepared thin film. For this range of sample parameters, we find the density profile in the heterojunction to be well approximated by

$$n(x) = \frac{C_{TG}V_{TG}}{1 + |x/w|^{2.5}} + C_{BG}V_{BG}, \quad (6)$$

where $w \sim 45\text{-}47$ nm is the effective width of the potential and the gate potentials V_{TG} and V_{BG} are coupled to the charge density through the capacitances $C_{TG} \approx 1490 \text{ aF}\mu\text{m}^2$ and $C_{BG} \approx 116 \text{ aF}\mu\text{m}^{-2}$. Here the exponent of x/w is chosen empirically, and produces a potential profile that deviates by less than 10% from that produced by the electrostatics simulations.

Fig. 4a shows density profiles in the graphene heterojunction which produce, via the Landauer formula described in the previous section, conductance fringes matching those observed in experiments done at $V_{BG} = 50$ V. From these density profiles, the potential profile, distance between classical turning points, and density gradient at the center of the p-n junctions is determined. We note that the distance between pn junctions, which determines the boundary of integration in equation (1), changes by a factor of two over the experimentally accessed density range, making the excellent quantitative fits obtained for the oscillation phase particularly convincing.

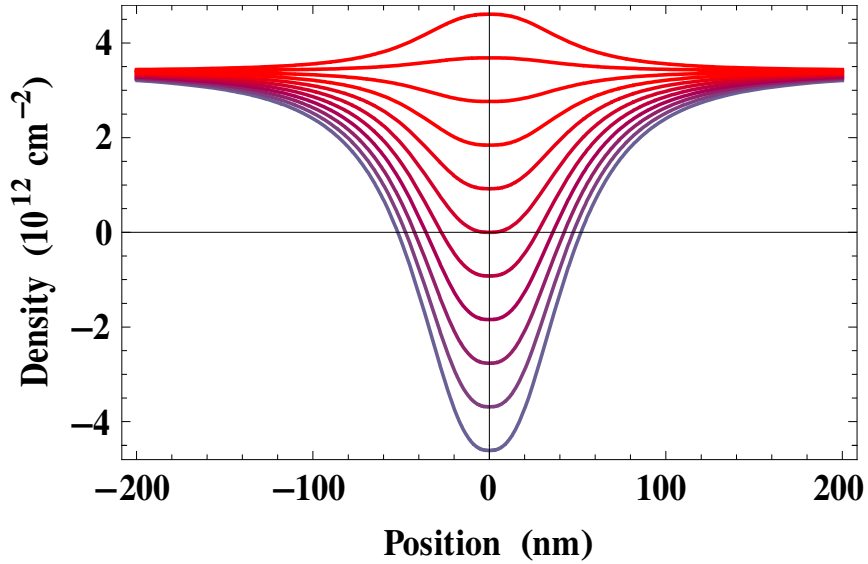


FIG. 1: Density profiles for $V_{BG} = 50$ V over a range of top gate voltages (from eq. 6). Top gate voltage in 1 V increments. The width of the central region (L) depends strongly on applied voltage.

C. Quantitative estimate of the electric field at the p-n interfaces

In this section, we compare the measured data (Fig. 5a) with numerical simulations to extract the strength of the electric field in an individual pn junction. It follows from robust semiclassical arguments² that, in the experimentally realized situation of p-n junctions smooth on the scale of the lattice constant, the collimation at an individual junction should be a Gaussian function of k_y (see eq. 3). The important parameter is the electric field, E , in the junctions, which is given, after taking into account the absence of linear screening in graphene near the charge neutrality point, by³

$$eE = 2.1\hbar v_F n'^{2/3}. \quad (7)$$

where n' is the density gradient across the junction. As is evident from the simulations (Fig. 5c), the nonlinear screening correction to the electric field gives a better fit to the experimental data than either the non-exponential collimation produced by atomically sharp barriers—which appears to contain higher order resonances—or the weaker field that results from neglecting nonlinear screening near the Dirac point.

To make this comparison more quantitative, we perform several simulations in which the nonlinear screening result, (7), is scaled by some prefactor, η . For a rough comparison, the linear screening corresponds to $\eta \lesssim .5$, while the step potential corresponds to $\eta \gg 20$. As explained in the main text, the magnetic field dependence contains an abrupt phase shift at finite magnetic field as the finite k_y modes cease to contribute to the oscillations and $k_y = 0$ modes—which carry with them the additional Berry phase of π —become the dominant contribution to the oscillatory conductance. With increasing magnetic field, a fully ballistic model predicts the gradual ebbing of these phase shifted oscillations as the cyclotron radius becomes comparable to the junction size. The field at which the π -phase shift manifests is tied to the degree of collimation of the transmission at each p-n interface. Because this phase shift is rather abrupt, we can define the transition magnetic field, B^* , as the field at which the values of the oscillation prefactor $|T_+|^2 |T_-|^2 |R_+| |R_-|$ for zero and finite k_y modes become comparable, giving $B^* \propto \sqrt{\frac{\hbar e E}{e^2 v_F L^2}}$. Since B^* depends strongly on the junction electric field, it allows us to extract this field from the experimentally observed oscillation phase shift. Defining B^* as the field at which $G_{osc}(n_2, B = B^*) = 0$ for fixed density n_2 such that $G_{osc}(n_2, B = 0)$ is an extremum, we can estimate $\eta = .9 \pm .3$.

In accordance with the ballistic theory, the oscillations peak at zero magnetic field, and then have a second maximum after the phase shift at finite magnetic field. The relative height of these two maxima can be used to estimate the electric field E . Higher collimation suppresses the contribution of the modes near $k_y = 0$ at finite B , since this feature is entirely generated by modes not normally incident at either interface. Higher collimation thus corresponds to an effectively more one-dimensional channel for interference effects, leading to the more effective destruction of the oscillations by the Lorentz force, which serves to push the particles out of the narrower acceptance angles at each junction. By taking the average value of G_B^{Max}/G_0^{Max} and comparing it with the simulations for a variety of values of η , we can extract $\eta \approx 1.6 \pm .3$. We note that the apparent discrepancy between this and the method previously outlined is likely due to the contribution of momentum non-conserving processes to the oscillations at finite B , leading to an overestimate of η . While neither of the methods above is free of systematic errors, they confirm the importance of nonlinear screening in determining transport through graphene p-n junctions.

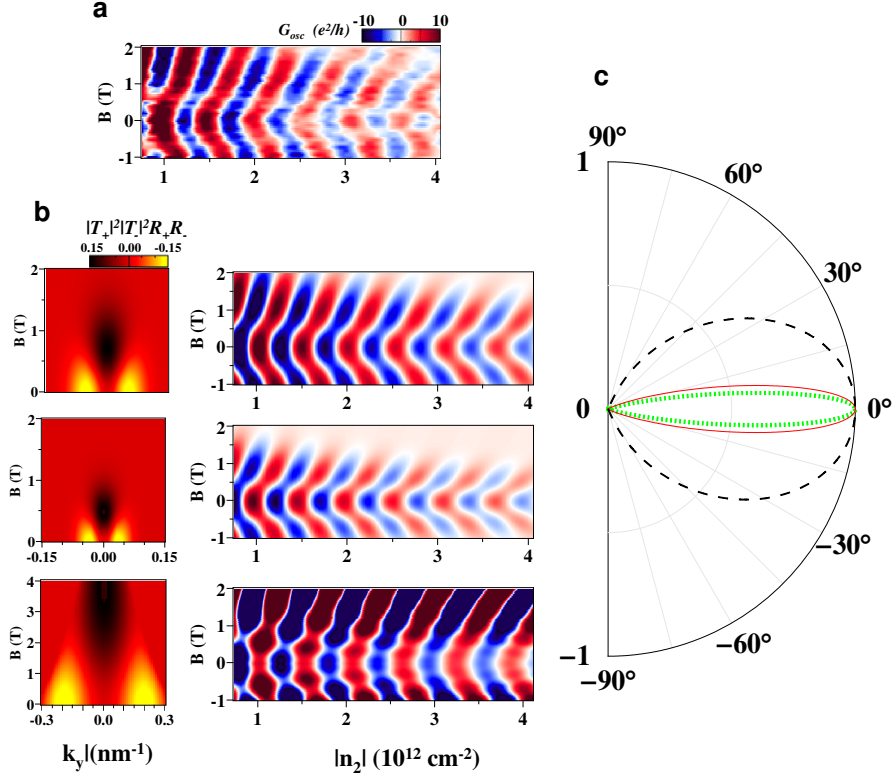


FIG. 2: **a** Top panel: oscillatory conductance as a function of n_2 and magnetic field at $V_{BG}=50\text{V}$. **b** The oscillation prefactor $|T_+|^2 |T_-|^2 R_+ R_-$ (column 1) and resulting oscillatory conductance (column 2) as a function of magnetic field for a variety of collimation models. The best fit to the data is achieved by accounting for the nonlinear screening (top panel); the simulations resulting from naively linearizing the potential between the extrema (middle panel) and considering the algebraic collimation resulting from a step potential (lower panel; note the different scale in left) show features incompatible with the observed data. The width of the central region is adjusted to be 46-48 nm in the simulations in order to match the phase of the zero field oscillations. The amplitude is fit by setting the mean free path in the Landauer formula to be 67 nm in the top panel, 60 nm in the central panel, and 300 nm for in the lower panel. **c** Transmission probability as a function of angle at zero magnetic field for the pn junctions with (red, solid) and without (green, dotted) nonlinear screening, and for the step potential (black, dashed).

D. Disordered heterojunctions

Several measured devices showed Fabry-Perot resonances; data from a second device (the same used in fig. 3d of the main text), is shown in Fig 6. Most of features discussed in text are present, including an oscillatory conductance that can be tuned by magnetic field. In this device, however, as in the majority of devices, the Fabry-Perot resonances appear to be mixed with other, irregular, conductance fluctuations. This behavior is most evident in the magnetic field dependence of the oscillations (Fig. 6c): although the phase shift is still evident in some of the transmission resonances, several oscillation periods appear to be intermixed, and there is no adiabatic crossover to the Shubnikov-de Haas oscillations as observed in the high quality device discussed in the main text. In addition, we discovered that the more disordered heterojunctions devices exhibit transmission resonances even when the overall doping of the LGR was of the same sign as that in the GL (Fig. 6b). We interpret these effects as a combination of higher disorder concentration between the p-n junctions causing enhanced mesoscopic conductance fluctuations and inhomogeneous gate coupling, which has the effect of causing an averaging over several Fabry Perot fringes.¹

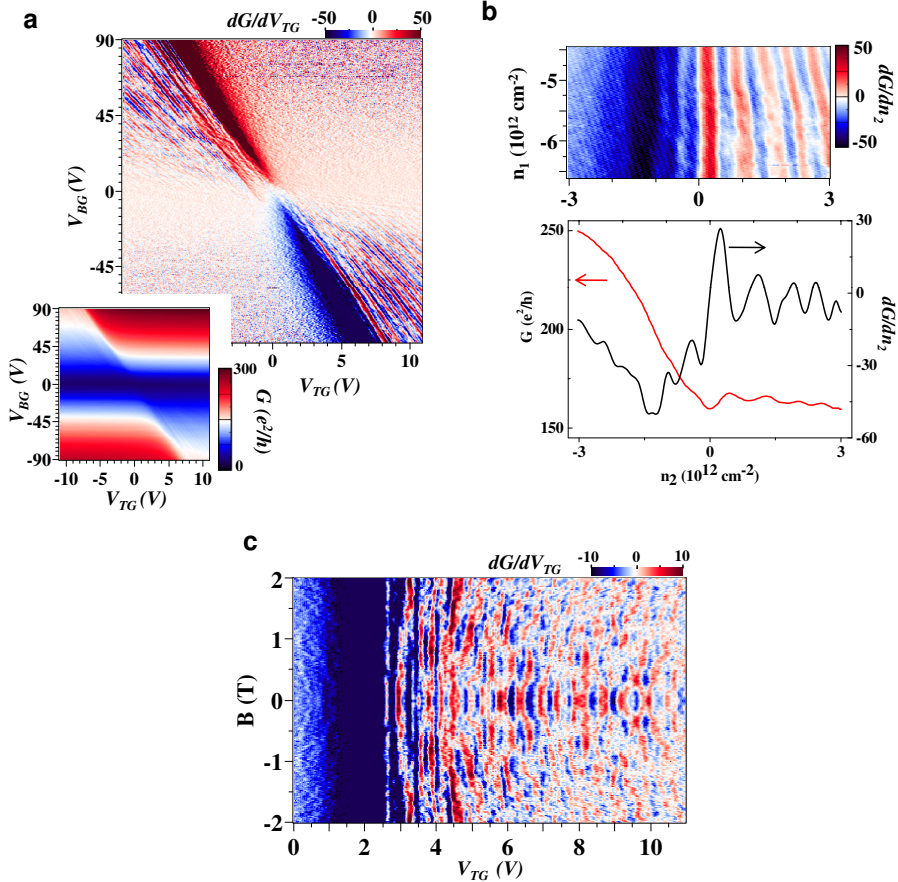


FIG. 3: Data from a second device. **a** Inset: Conductance, measured in the four wire geometry, as a function of top and back gate voltages. Main Panel: Derivative of conductance with respect to top gate voltage (arbitrary units). **b** Oscillations in the unipolar regime. The oscillations are visible in the derivative of the conductance with respect to top gate voltage, and as kinks in the steeply falling background conductance as the central region approaches charge neutrality. **c** The irregular character of the oscillations becomes apparent in the magnetic field dependence of the oscillation extrema. Although the phase shift is still visible, several periods seem intermixed, and there is no apparent adiabatic connection to the Shubnikov-de Haas oscillations.

- ¹ Shytov, A.V., Rudner, M.S., & Levitov, L.S. Klein Backscattering and Fabry-Perot Interference in Graphene Heterojunctions. To appear in *Phys. Rev. Lett.* (2008).
- ² Cheianov, V.V. & Fal'ko, V.I. Selective transmission of Dirac electrons and ballistic magnetoresistance of n-p junctions in graphene. *Phys. Rev. B* **74**, 041403(R) (2006).
- ³ Zhang, L.M. & Fogler, M.M. Nonlinear Screening and Ballistic Transport in a Graphene p-n Junction. *Phys. Rev. Lett.* **100**, 116804 (2008).
- ⁴ Ryu, S., et al. Reversible Basal Plane Hydrogenation of Graphene. *Nano Letters* **8** (12) pp. 45974602 (2008).